Variable Switching Sequence PWM Strategy of Dual Three-Phase Machine Drive for High-Frequency Current Harmonic Suppression

Donglin Ye, *Student Member, IEEE*, Jian Li, *Senior Member, IEEE*, Ronghai Qu, *Fellow, IEEE*, Dong Jiang, *Senior Member, IEEE*, Lifan Xiao, *Student Member, IEEE*, Yang Lu, *Student Member, IEEE*, and Junhua Chen, *Senior Member, IEEE*

***Abstract*—The circulating current harmonics are inherent disadvantages of dual three-phase machines, resulting in additional copper losses, severe current distortions, and high switching ripples. Traditional strategies offer many methods to suppress low-order current harmonics but pay little attention to the high-frequency harmonics and the performance improvement over one pulsewidth-modulation (PWM) cycle. Because of the ability of model predictive PWM (MPP) technique to predict real-time current ripples, this article proposes a variable switching sequence PWM (VSSPWM) strategy to optimize the current harmonic in a PWM period. The proposed method derives current ripples to predict real-time trajectories and root-mean-square (rms) values of current harmonics. By this means, VSSPWM can be implemented based on the enumeration and evaluation of all admissible switching sequence patterns. The cost function is designed to evaluate the rms current and select the optimal switching sequence. Simulation and experimental results have verified the effectiveness of the proposed strategy that VSSPWM can provide good high-frequency current harmonics suppression performance.**

***Index Terms*—Circulating current harmonic, high-frequency suppression, multiphase drives, prediction, pulsewidth modulation (PWM).**

I. Introduction

In THE past two decades, dual three-phase machines, or asymmetrical six-phase machines, have received extensive attention since they can offer many important advantages when compared with conventional three-phase counterparts, such as fault-tolerant capability, low torque ripple, low vibration, and low dc-link current ripple [1], [2]. Dual three-phase machines are applied in high-power and high-reliability areas, such as electric vehicles, ship pulsations, and more-electric aircraft [3].

Manuscript received April 29, 2019; revised July 25, 2019; accepted September 11, 2019. Date of publication September 16, 2019; date of current version February 11, 2020. This work was supported in part by the National Natural Science Foundation of China under Grant 51877094, and in part by the National Key R&D Program of China under Grant 2016YF1200601. Recommended for publication by Associate Editor N. Zargari. *(Corresponding author: Jian Li.)*

The authors are with the State Key Laboratory of Advanced Electromagnetic Engineering and Technology, School of Electrical and Electronic Engineering, Huazhong University of Science and Technology, Wuhan 430074, China (e-mail: yedonglin@hust.edu.cn; jianli@hust.edu.cn; ronghaiqu@hust.edu.cn; jiangd@hust.edu.cn; lifanxiao@hust.edu.cn; luyang@hust.edu.cn).

Color versions of one or more of the figures in this article are available online at http://ieeexplore.ieee.org.

Digital Object Identifier 10.1109/TPEL.2019.2941991

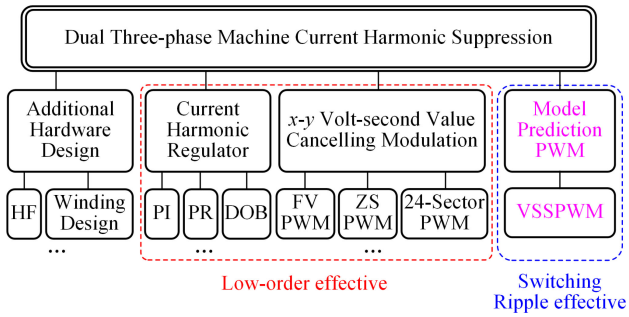

Fig. 1. Category of circulating current harmonic suppression methods for dual three-phase machines.

The dual three-phase machine has a drawback that there are circulating current harmonics flowing in the stator windings. These circulating current harmonics are mapped into the $x-y$ subspace according to the vector space decomposition (VSD) theory, which are known as the $6k \pm 1$th ($k = 1, 3, 5, \ldots$) harmonics [4], and they are not involved in the electromechanical energy conversion but cause extra copper losses and the degradations of total harmonic distortions (THD). The circulating currents also lead to the unbalance within phase currents according to the work presented in [5]. Besides, when the order of the circulating current harmonic is near the switching frequency, it brings in severe machine high-frequency vibration and noise [6]. These high-frequency current harmonics will be inevitably large because the impedance in the $x-y$ subspace only consists of the stator resistance and the leakage inductance [7].

The previous circulating current harmonics suppression strategies, which can be summarized as the first three groups in Fig. 1, pay lots of attention to the low-order $x-y$ current suppressions. The first group of approaches is to add harmonic filter or modify the winding structure to reduce the current harmonics [8], [9], but this kind of method will increase the complexity and cost of the drive system. The second group is to use current harmonic regulators. The proportional–integral (PI) regulator and proportional–resonant (PR) regulator have been used for the control of $x-y$ current in a synchronous or stationary reference [4], [5], [10]. The disturbance observer has also been used for the current harmonic suppression, which has both good robustness and steady-state performance [2].

However, current harmonic regulators cannot control the high-frequency current harmonics, whose frequencies are usually far greater than the control frequency. The third group is to use the pulsewidth-modulation (PWM) strategy to suppress current harmonics by making the $x-y$ volt–second value zero [11]–[15]. This kind of strategy includes modulation methods such as four-vector PWM (FVPWM), double zero sequence-injection PWM (ZSPWM), 24-sector space vector PWM (24-Sector PWM), and so on. Since this kind of method is based on the principle of zero volt–second value in one PWM period, it can only suppress low-order current harmonics, but cannot improve harmonic performances within the PWM cycle.

In order to suppress the high-frequency current harmonics near the switching frequency, this article proposes a variable switching sequence PWM (VSSPWM) strategy based on the model predictive PWM (MPP) theory as the fourth group of suppressing approaches depicted in the blue box in Fig. 1. MPP is a technique based on the real-time prediction model of related physical quantities, which can make full use of PWM freedom to effectively improve the modulation performance [16]–[18]. Jiang and Wang [16] proposed the current ripple prediction method for voltage-source inverters (VSI), which can calculate the current ripple trajectory in real time. Yang *et al.* [17] used MPP to predict dq-axis current ripples in the three-phase rotating system. Considering the excellent characteristics of MPP, if the circulating current harmonics can be predicted, the switching sequence of the dual three-phase VSIs can be optimized in real time. Thereby, the current performance in one PWM cycle can be improved, even further the dc-link current ripples can be optimized [18].

The rest of this article is organized as follows. In Section I, the circulating current prediction model is proposed, and the contributions of the two sets of windings to the circulating current harmonics are analyzed. In Section II, based on the current prediction model, the circulating current prediction method and the VSSPWM strategy are proposed in detail. In Section III, the proposed strategy is implemented in a dual three-phase drive through MATLAB/Simulink, and the steady-state performance is compared with the classical FVPWM method in detail. In Section IV, the experimental results are given to verify the superiority of the proposed VSSPWM, and the performance in the dynamic process is also analyzed. Finally, the conclusions are drawn in Section V.

II. Circulating Current Prediction Model

The power circuit of the dual three-phase permanent-magnet synchronous machine (PMSM) drive is shown in Fig. 2. The neutrals of the two sets of windings abc and uvw are isolated to avoid the appearance of the $3k$th, $(k=0,1,3,5,\ldots)$, current harmonics.

The synchronous frame quantities can be obtained from the stationary phase quantities using the VSD theory in [19] as

$$\boldsymbol{F_r} = \boldsymbol{T_{VSD}} \cdot \boldsymbol{F_s} \tag{1}$$

where

$$\boldsymbol{F_r} = [F_d, F_q, F_{dz}, F_{qz}, F_{o1}, F_{o2}]^{\intercal}$$

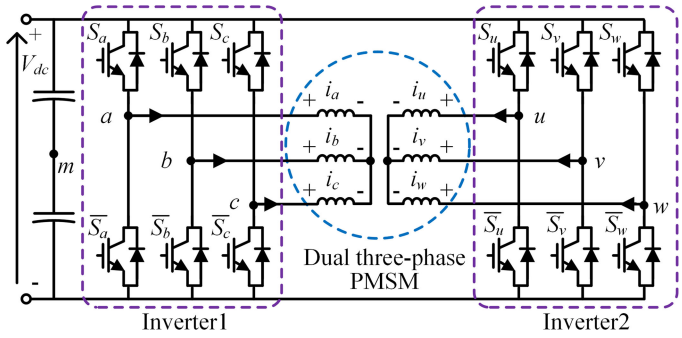

Fig. 2. Power circuit of the dual three-phase PMSM drive.

$$\boldsymbol{F_s} = [F_a, F_b, F_c, F_u, F_v, F_w]^{\intercal} \tag{2}$$

and F stands for machine voltage v, current i, and flux linkage λ. The d- and q-axis are the synchronized frame transformed from α- and β-axis stationary frame, dz- and qz-axis are the synchronized frame transformed from x- and y-axis stationary frame, and $o1$- and $o2$- are the stationary frame containing zero-sequences [19]. More details about VSD theory are given in the Appendix.

The VSD transform matrix in (1) can be expressed as

$$\boldsymbol{T_{VSD}}(\theta) = \begin{bmatrix} \boldsymbol{T_{dq1}}(\theta) & \boldsymbol{T_{dq2}}(\theta) \\ \boldsymbol{T_{dqz1}}(\theta) & \boldsymbol{T_{dqz2}}(\theta) \\ \boldsymbol{T_{o1}} & \boldsymbol{T_{o2}} \end{bmatrix} \tag{3}$$

where θ is the electrical displacement of the d-axis from the a winding magnitude axis, and

$$\begin{aligned}
\boldsymbol{T_{dq1}}(\theta) &= \sqrt{\frac{1}{3}} \begin{bmatrix} \cos(\theta) & \cos(\theta-4\alpha) & \cos(\theta-8\alpha) \\ -\sin(\theta) & -\sin(\theta-4\alpha) & -\sin(\theta-8\alpha) \end{bmatrix} \\
\boldsymbol{T_{dqz1}}(\theta) &= \sqrt{\frac{1}{3}} \begin{bmatrix} -\cos(\theta) & -\cos(\theta-4\alpha) & -\cos(\theta-8\alpha) \\ \sin(\theta) & \sin(\theta-4\alpha) & \sin(\theta-8\alpha) \end{bmatrix} \\
\boldsymbol{T_{dq2}}(\theta) &= \boldsymbol{T_{dq1}}(\theta-\alpha), \quad \boldsymbol{T_{dqz2}}(\theta) = -\boldsymbol{T_{dqz1}}(\theta-\alpha) \\
\boldsymbol{T_{o1}} &= \sqrt{\frac{1}{3}} \begin{bmatrix} 1 & 1 & 1 \\ 0 & 0 & 0 \end{bmatrix}, \boldsymbol{T_{o2}} = \sqrt{\frac{1}{3}} \begin{bmatrix} 0 & 0 & 0 \\ 1 & 1 & 1 \end{bmatrix}
\end{aligned} \tag{4}$$

where $\alpha = \pi/6$, and the subscripts 1 and 2 stand for abc and uvw windings, respectively.

Therefore, the dz- and qz-axis quantities are calculated as

$$\begin{aligned}
\boldsymbol{F_{dqz}} &= \boldsymbol{F_{dqz1}} + \boldsymbol{F_{dqz2}} \\
&= \begin{bmatrix} F_{dz1} + F_{dz2} \\ F_{qz1} + F_{qz2} \end{bmatrix} = \boldsymbol{T_{dqz1}}(\theta) \begin{bmatrix} F_a \\ F_b \\ F_c \end{bmatrix} + \boldsymbol{T_{dqz2}}(\theta) \begin{bmatrix} F_u \\ F_v \\ F_w \end{bmatrix}
\end{aligned} \tag{5}$$

where $\boldsymbol{F_{dqz}} = [F_{dz}, F_{qz}]^{\intercal}$, and $\boldsymbol{F_{dqz(n)}} = [F_{dz(n)}, F_{qz(n)}]^{\intercal}$, $(n=1,2)$.

Further, (5) can be rewritten as

$$\begin{bmatrix} F_{dz1} \\ F_{qz1} \\ F_{dz2} \\ F_{qz2} \end{bmatrix} = \underbrace{\begin{bmatrix} \boldsymbol{T_{dqz1}}(\theta) & \boldsymbol{0_{2\times 3}} \\ \boldsymbol{0_{2\times 3}} & \boldsymbol{T_{dqz2}}(\theta) \end{bmatrix}}_{\boldsymbol{T_{dqz}(\theta)}} \begin{bmatrix} F_a \\ F_b \\ F_c \\ F_u \\ F_v \\ F_w \end{bmatrix}. \tag{6}$$

The voltage equation in the natural frame is expressed as

$$\boldsymbol{v_r} = R_r \boldsymbol{i_r} + \boldsymbol{L_r}\frac{d\boldsymbol{i_r}}{dt} + \frac{d\boldsymbol{\lambda}_r(\theta)}{dt} \tag{7}$$

where R_r is the stator resistance and $\boldsymbol{L_r}$ is the stator inductance, which can be expressed as

$$\boldsymbol{L_r} = \begin{bmatrix} \boldsymbol{L_{11}} & \boldsymbol{M_{12}} \\ \boldsymbol{M_{21}} & \boldsymbol{L_{22}} \end{bmatrix} \tag{8}$$

where $\boldsymbol{L_{11}}$ and $\boldsymbol{L_{22}}$ are the inductance matrices within the two sets of windings, and $\boldsymbol{M_{12}}$ and $\boldsymbol{M_{21}}$ are the mutual inductance matrices between the two sets of windings. A more detailed description of these inductances can be found in [20].

Applying (6) to (8), the resulting inductance matrix $\boldsymbol{L_{dqz}}$, related to the two orthogonal $dz1-qz1$ and $dz2-qz2$ frames, can be calculated as

$$\begin{aligned} \boldsymbol{L_{dqz}} &= \boldsymbol{T_{dqz}}(\theta)\cdot \boldsymbol{L_s}\cdot \boldsymbol{T_{dqz}}^{\intercal}(\theta) \\ &= \begin{bmatrix} L_{dz1} & 0 & M_{dz12} & 0 \\ 0 & L_{qz1} & 0 & M_{qz12} \\ M_{dz21} & 0 & L_{dz2} & 0 \\ 0 & M_{qz21} & 0 & L_{qz2} \end{bmatrix} \end{aligned} \tag{9}$$

with

$$\begin{aligned} L_{dz1} &= L_{dz2} = L_{s0} + L_{s2}/2 - M_{s0} + M_{s2} \\ L_{qz1} &= L_{qz2} = L_{s0} - L_{s2}/2 - M_{s0} - M_{s2} \\ M_{dz12} &= M_{dz21} = -3\left(M_{m0} + M_{Mm2}\right)/2 \\ M_{qz12} &= M_{qz21} = -3\left(M_{m0} - M_{Mm2}\right)/2 \end{aligned} \tag{10}$$

where L_{s0} and L_{s2}, M_{s0} and M_{s2}, M_{m0} and M_{m2} are the average values and second-order amplitudes of the self-inductance, mutual inductance within one set of windings, and mutual inductance between two sets of windings, respectively.

According to the work presented in [17], the voltage or current F during one PWM cycle consists of the average component $\overline{F}$ and the ripple component ΔF, which can be expressed as

$$F = \overline{F} + \Delta F. \tag{11}$$

Substituting (11) into (7), the voltage equation is shown as

$$\left(\overline{\boldsymbol{v}}_{\boldsymbol{r}} + \Delta\boldsymbol{v_r}\right) = R_r\left(\overline{\boldsymbol{i}}_{\boldsymbol{r}} + \Delta\boldsymbol{i_r}\right) + \boldsymbol{L_r}\frac{d}{dt}\left(\overline{\boldsymbol{i}}_{\boldsymbol{r}} + \Delta\boldsymbol{i_r}\right) + \frac{d\boldsymbol{\lambda}_r(\theta)}{dt}. \tag{12}$$

Hence, the equations of the voltage average and the voltage ripple can be obtained, respectively, as follows:

$$\overline{\boldsymbol{v}}_{\boldsymbol{r}} = R_r\overline{\boldsymbol{i}}_{\boldsymbol{r}} + \boldsymbol{L_r}\frac{d\overline{\boldsymbol{i}}_{\boldsymbol{r}}}{dt} + \frac{d\boldsymbol{\lambda}_r(\theta)}{dt} \tag{13}$$

$$\Delta\boldsymbol{v_r} = R_r\Delta\boldsymbol{i_r} + \boldsymbol{L_r}\frac{d\Delta\boldsymbol{i_r}}{dt}. \tag{14}$$

By ignoring the voltage drop on the resistance in (14), the voltage ripple equations can be expressed as

$$\Delta\boldsymbol{v_r} = \boldsymbol{L_r}\frac{d\Delta\boldsymbol{i_r}}{dt}. \tag{15}$$

Applying (6) to (15), the voltage equation is rewritten as

$$\boldsymbol{T_{dqz}}\Delta\boldsymbol{v_r} = \boldsymbol{T_{dqz}}\begin{bmatrix} \boldsymbol{L_{11}} & \boldsymbol{M_{12}} \\ \boldsymbol{M_{21}} & \boldsymbol{L_{22}} \end{bmatrix}\boldsymbol{T_{dqz}}^{\intercal}\cdot\boldsymbol{T_{dqz}}\frac{d}{dt}\Delta\boldsymbol{i_r}. \tag{16}$$

Substituting (9) into (16), the result can be calculated as

$$\begin{bmatrix} \Delta v_{dz1} \\ \Delta v_{dz2} \\ \Delta v_{qz1} \\ \Delta v_{qz2} \end{bmatrix} = \begin{bmatrix} L_{dz1} & 0 & M_{dz12} & 0 \\ 0 & L_{qz1} & 0 & M_{qz12} \\ M_{dz21} & 0 & L_{dz2} & 0 \\ 0 & M_{qz21} & 0 & L_{qz2} \end{bmatrix}\frac{d}{dt}\begin{bmatrix} \Delta i_{dz1} \\ \Delta i_{dz2} \\ \Delta i_{qz1} \\ \Delta i_{qz2} \end{bmatrix}. \tag{17}$$

Finally, the circulating current ripple slope is obtained as

$$\frac{d}{dt}\begin{bmatrix} \Delta i_{dz1} \\ \Delta i_{dz2} \\ \Delta i_{qz1} \\ \Delta i_{qz2} \end{bmatrix} = \begin{bmatrix} \frac{L_{dz2}}{K_1} & 0 & \frac{M_{dz12}}{-K_1} & 0 \\ 0 & \frac{L_{qz2}}{K_2} & 0 & \frac{M_{qz12}}{-K_2} \\ \frac{M_{dz12}}{-K_1} & 0 & \frac{L_{dz1}}{K_1} & 0 \\ 0 & \frac{M_{qz12}}{-K_2} & 0 & \frac{L_{qz1}}{K_2} \end{bmatrix}\begin{bmatrix} \Delta v_{dz1} \\ \Delta v_{dz2} \\ \Delta v_{qz1} \\ \Delta v_{qz2} \end{bmatrix} \tag{18}$$

where

$$\begin{aligned} K_1 &= L_{dz1}L_{dz2} - M_{dz12}^2 \\ K_2 &= L_{qz1}L_{qz2} - M_{qz12}^2. \end{aligned} \tag{19}$$

It can be seen from (18) and (19) that the voltage ripple of the corresponding set of windings (1 or 2) only affects the dqz currents with the same number, and the greater of the two sets of windings' coupling, which means the greater M_{dz12} and M_{qz12}, the more significant the effect of this voltage ripple.

III. VSSPWM for Circulating Current Control

A. Basic Principle

The VSSPWM is a strategy for optimizing the switching sequence of a basic modulation method, which can be FVPWM, ZSPWM, 24-Sector PWM, etc. After VSSPWM adopts a certain basic modulation strategy, the vectors participating in the modulation and their active time can be determined, and the number of admissible switching sequences is finite when several design principles are followed. Then, at each sampling instant, the possible switching sequences are enumerated, and the corresponding modulation performance during this whole PWM cycle could be predicted. A cost function is designed to evaluate the modulation performance of each prediction, and the one that yields the minimal cost is selected. The flow diagram of the VSSPWM strategy is shown in Fig. 3.

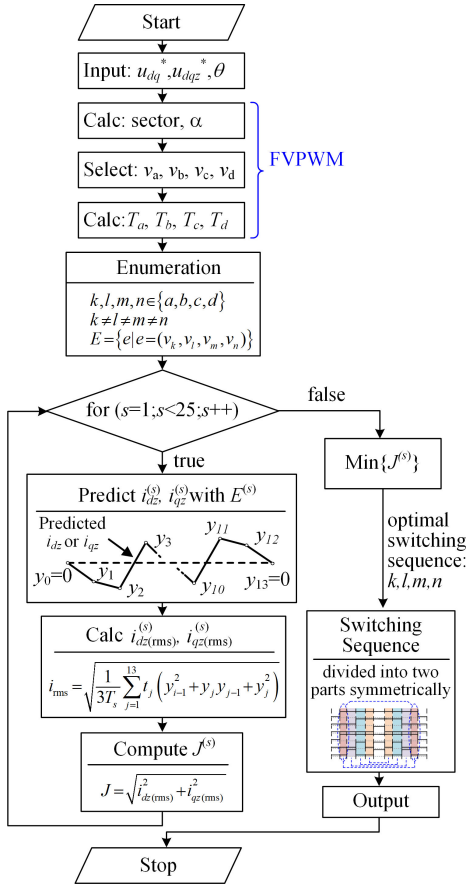

Fig. 3. Flow diagram of the FVPWM-based VSSPWM strategy.

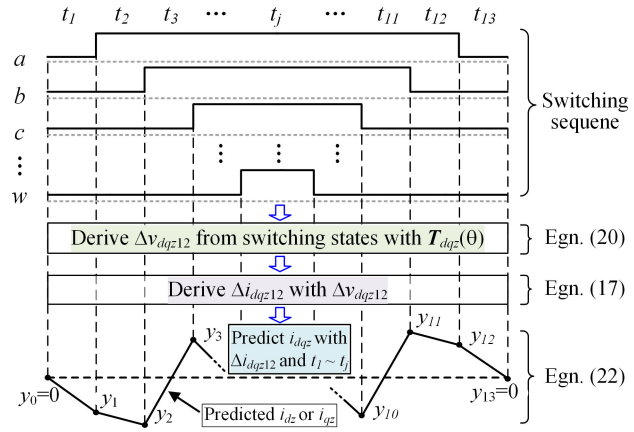

Fig. 4. i_{dqz} prediction process in one PWM cycle for a general PWM pattern.

B. Circulating Current Prediction

Based on the circulating current slope model (18), the circulating current ripple can be predicted in real time. Because the average value of the circulating current is zero, the circulating current ripple refers to the circulating current itself.

In Fig. 2, m is the midpoint of the dc-link voltage. The inverter pole voltage v_{im}, $(i = a \sim w)$ has two values, i.e., $V_{\mathrm{dc}}/2$ and $-V_{\mathrm{dc}}/2$, which is decided by the switching state. Thereby, the pole voltage can be decomposed into the average component $\overline{v}_{im}$ and the ripple component Δv_{im}.

Since $\overline{v}_{im}$ can be decided with the duty-cycle D_i, $(i = a \sim w)$ of the inverter leg, i.e., $\overline{v}_{im} = (2D_i - 1)V_{\mathrm{dc}}/2$, the voltage ripple can be computed as

$$\Delta v_{im} = \begin{cases} V_{\mathrm{dc}}/2 - \overline{v}_{im} = V_{\mathrm{dc}}(1 - D_i), & \text{if } S_i \text{ is ON} \\ -V_{\mathrm{dc}}/2 - \overline{v}_{im} = -V_{\mathrm{dc}} D_i, & \text{if } S_i \text{ is OFF.} \end{cases} \tag{20}$$

Applying (6) to (20), the voltage ripple can be obtained as

$$\Delta \boldsymbol{v}_{\boldsymbol{dqz12}} = \boldsymbol{T}_{\boldsymbol{dqz}}(\theta) \Delta \boldsymbol{v}_{\boldsymbol{sm}} \tag{21}$$

where

$$\begin{aligned} \Delta \boldsymbol{v}_{\boldsymbol{dqz12}} &= [\Delta v_{dz1}, \Delta v_{qz1}, \Delta v_{dz2}, \Delta v_{qz2}]^{\mathsf{T}} \\ \Delta \boldsymbol{v}_{\boldsymbol{sm}} &= [\Delta v_{am}, \Delta v_{bm}, \Delta v_{cm}, \Delta v_{um}, \Delta v_{vm}, \Delta v_{wm}]^{\mathsf{T}}. \end{aligned} \tag{22}$$

Consequently, by using (18) and (21) the circulating current slope can be computed. The dqz-axis current is the sum of the $dqz1$- and $dqz2$-axis currents, which can be obtained by integrating the current slopes with time. The calculation of i_{dqz} is shown as

$$i_{dqz} = i_{dqz1} + i_{dqz2} = \sum_{n=1,2} \left(\sum_{j=1}^{13} \left(\left. \frac{d\Delta i_{dqz(n)}}{dt} \right|_j \cdot t_j \right) \right) \tag{23}$$

where $\Delta i_{dqz(n)} = [\Delta i_{dz(n)}, \Delta i_{qz(n)}]^{\mathsf{T}}$, $(n = 1, 2)$, j, $(j = 1, 2, \ldots, 13)$, is the number of the vector sequence in one PWM cycle, and t_j is the active time of the corresponding vector.

The circulating current prediction procedure is illustrated in Fig. 4 for a general PWM pattern of dual three-phase machine drives. The y_j, $(j = 0, 1, \ldots, 13)$, is the peak value of the current ripple, which can be calculated with (23). Since the average value of i_{dqz} is zero, y_0 and y_{13} both equal to zero. Based on the (23) and Fig. 4, the root-mean-square (rms) value of the circulating current can also be predicted, which is calculated as

$$i_{\mathrm{rms}} = \sqrt{\frac{1}{3T_s} \sum_{j=1}^{13} t_j \left(y_{j-1}^2 + y_j y_{j-1} + y_j^2 \right)} \tag{24}$$

where i_{rms} can be the rms values of dz-axis current $i_{dz(\mathrm{rms})}$ or qz-axis current $i_{qz(\mathrm{rms})}$.

C. Optimization Objectives

In order to suppress the current harmonic during each PWM cycle, the cost function is designed to evaluate the total rms value of current harmonics i_{dz} and i_{qz}. The cost function is designed as

$$J = \sqrt{i_{dz(\mathrm{rms})}^2 + i_{qz(\mathrm{rms})}^2}. \tag{25}$$

The principle of the MPP in VSSPWM is shown in Fig. 6. Among the 24 switching sequences, the one that yields the minimum cost is selected as the optimal switching sequence.

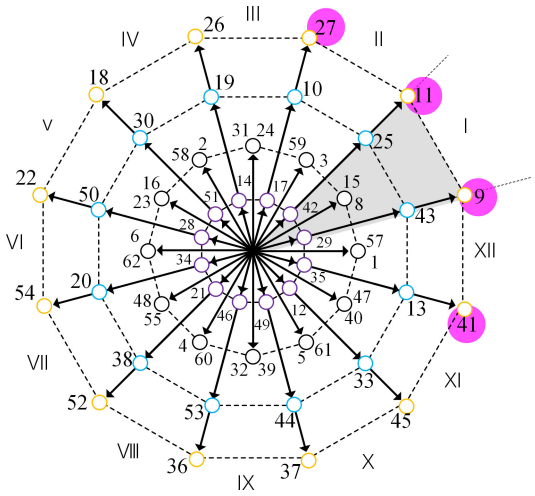

Fig. 5. 64 vectors of the dual three-phase drive in the $\alpha\beta$ subspace, and the selected four outermost large vectors in sector I.

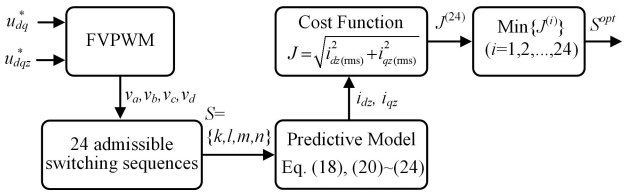

Fig. 6. Principle of model predictive PWM in VSSPWM for selecting the optimal switching sequence.

D. Switching Pattern Design Principle

A basic modulation method needs to be decided before implementing VSSPWM. In this article, the FVPWM is selected, since FVPWM is the most common modulation method for dual three-phase machine drives, which uses four outermost large vectors to synthesize the vector reference. Also, the four large vectors give VSSPWM a lot of degrees of freedom for switching sequence optimization. The design principle is listed as follows.

1) Vectors involved: The four adjacent outermost vectors are selected. FVPWM divides the 64 vectors into 12 sectors. Taking the sector I as the example as shown in Fig. 5, the vectors 41, 9, 11, and 27 are selected.

2) Symmetry: The PWM waveform of traditional FVPWM is asymmetrical for low-switching losses as shown in Fig. 7(a). However, this asymmetry introduces other harmonics and is difficult to implement [11]. Thus, the PWM waveform is always symmetrized without changing the duty cycles. Taking sector I as an example that the original vectors are 41, 9, 11, and 27, and after symmetrizing, the vectors are 11, 9, 43, and 59 as shown in Fig. 7(b). For this reason, the VSSPWM has also been designed with symmetry, by distributing each vector symmetrically in the PWM cycle as shown in Fig. 7(c). The active times of v_{41}, v_9, v_{11}, and v_{27} are t_1, t_2, t_3, and t_4 respectively, and they are divided into two parts and symmetrically distributed.

3) Cancellation Mechanism: Due to the characteristic of semiconductor devices, the PWM pulse that is too narrow may cause the missing of switch actions. This happens when the modulation index (MI) is low or high for the VSSPWM and would result in the wrong PWM output. In order to avoid wrong switching states, the rising- and falling-edges with too short intervals should be cancelled together. The critical interval for cancellation is set to be $T_{\min}$. The cancellation mechanism is shown in Fig. 8.

Assuming that the edges time interval is ΔT, when $\Delta T > T_{\min}$, no PWM pulses will be missing as shown in Fig. 8(a). When $\Delta T < T_{\min}$, if the cancellation mechanism does not work, the falling edge will be missed and the wrong PWM waveform will be output as shown in Fig. 8(b). If the cancellation mechanism works, the two actions will be cancelled as shown in Fig. 8(c), so that the right PWM waveform can be obtained. The cancellation mechanism will cause little PWM waveform errors since the duty cycle is changed a little. This error is easily compensated by adjusting the duty cycle of the intermediate PWM pulse as shown in Fig. 8(d).

Algorithm 1: Enumerate, predict and evaluate admissible switching sequences.

Input: v_a, v_b, v_c, v_d
Output: $J^{(s)}$

```
v1 ⇐ va, v2 ⇐ vb, v3 ⇐ vc, v4 ⇐ vd
i ⇐ 1, s ⇐ 1
if i ≤ 4 then
  j ⇐ 1
  if j ≤ 4 && j ≠ i then
    o ⇐ 1
    if o ≤ 4 && o ≠ j && o ≠ i then
      p ⇐ 1
      if p ≤ 4 && p ≠ o && p ≠ j && p ≠ i then
        (vk, vl, vm, vn) ⇐ (vi, vj, vo, vp)
        compute i^(s)_dqz and J^(s) with (vk, vl, vm, vn)
        s ⇐ s + 1
        p ⇐ p + 1
      end if
      o ⇐ o + 1
    end if
    j ⇐ j + 1
  end if
  i ⇐ i + 1
end if
```

E. Enumeration Procedure

The admissible switching sequences with the four vectors that the conventional FVPWM used are enumerated. Assuming that the vectors selected by FVPWM are v_a, v_b, v_c, and v_d, the enumeration procedure is illustrated in Algorithm 1.

F. Robustness Discussion

The $x-y$ impedance only consists of stator resistance and harmonic inductance, and the harmonic inductance is induced by the leakage flux whose magnetic circuit only passes across

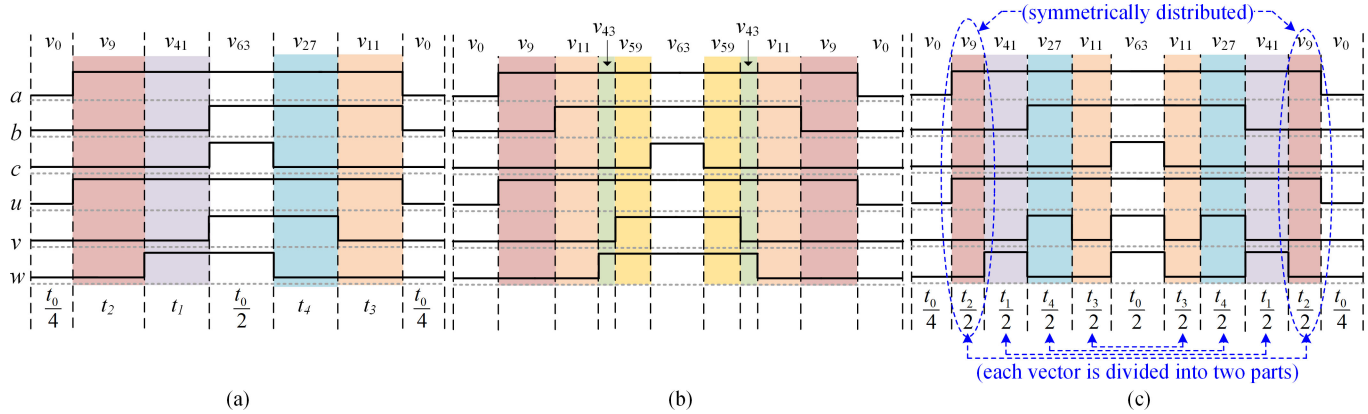

Fig. 7. PWM waveforms in sector I of (a) asymmetrical FVPWM, (b) symmetrical FVPWM, and (c) VSSPWM (one of the admissible switching sequences).

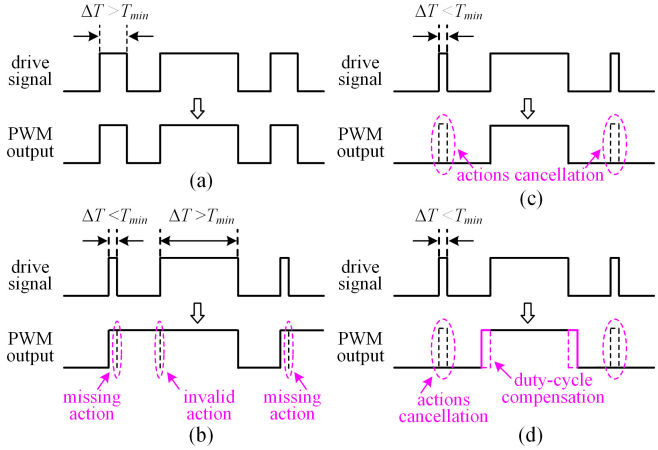

Fig. 8. PWM waveforms cancellation mechanism. (a) Normal condition ($\Delta T > T_{\min}$). (b) Missing pulses condition ($\Delta T < T_{\min}$) with no cancellation mechanism. (c) Missing pulses condition ($\Delta T < T_{\min}$) with cancellation mechanism. (d) Cancellation with duty-cycle compensation.

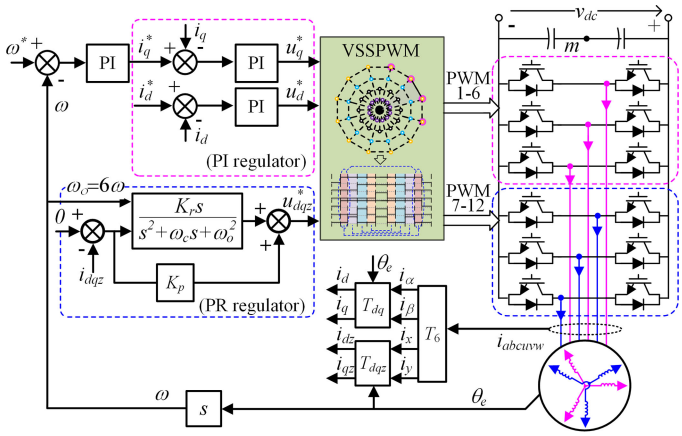

Fig. 9. Control block diagram of the VSSPWM controlled dual three-phase machine drive.

stator teeth [9], [21]. The harmonic inductances can be expressed as [9]

$$L_{dz} = L_{qz} = L_{ls} - M_{ls} - \frac{3}{2}M_{lm} = L_t + L_b + 2M_{tb}\left[1 - \left(\frac{\sqrt{3}}{2} + 1\right)k\right], (k = (1-r)mq). \tag{26}$$

Further, the relationship in the following is easy to be obtained:

$$\begin{aligned} L_{dz} &= L_{dz1} + M_{dz12} \\ L_{qz} &= L_{qz1} + M_{qz12} \end{aligned} \tag{27}$$

where L_{ls}, M_{ls}, and M_{lm} are the leakage inductances of L_s, M_s, and M_m, respectively, L_t, L_b, and M_{tb} are the self-leakage inductances related to the top and bottom conductors and mutual leakage inductance between the two conductors, respectively, r is the coil pitch, q is the slots per phase, and m the number of phases.

Hence, the harmonic impedance would not be influenced by the saturation effect of the main magnetic circuit. Since the current ripple prediction only uses leakage inductances, VSSPWM will have good robustness when the machine is under different load conditions.

G. Control Method for Dual Three-Phase Machine Drive

The control block diagram of the VSSPWM controlled dual three-phase machine drive is shown in Fig. 9. The control block consists of five closed loops, i.e., one outer speed loop and four inner current loops. The four current closed loops are two PI regulator controlled *dq* current closed loops and two PR regulator controlled *dqz* current closed loops. In maximum torque per ampere (MTPA) condition, the i_d^* equals zero in this paper. Since the i_{dqz} mainly contains the sixth current harmonics, the resonant frequency ω_o is set to be six times of machine electrical frequency ω, i.e., $\omega_o = 6\omega$. After several trials, the PI parameters for *dq* currents are set to $K_p = 0.5$ and $K_i = 30$. For the PR regulator, K_r is the gain of the resonant term, which is set to $K_r = 4400$, and ω_c is the bandwidth, which is set to 20 rad/s. The proportional gain of PR regulator is set to $K_p = 1.5$.

TABLE I
PARAMETERS OF THE PROTOTYPE DUAL THREE-PHASE PMSM

Parameters	Values
Number of poles	10
Number of slots	12
PM flux linkage (Wb)	0.047
Phase resistance (Ω)	0.244
Self-inductance L_s (mH)	1.3
Rated phase current RMS value (A)	7
Mutual-inductance M_s (mH)	0
Rated velocity (r/min)	1200
Mutual-inductance M_m (mH)	0.18
Rated torque (N·m)	7

IV. SIMULATION RESULTS

In order to study the proposed VSSPWM strategy, it is compared in detail with the conventional FVPWM and the symmetrized FVPWM under the condition of the same switching frequency. It is confirmed in the simulation that the average switching frequency (f_{sw}) of the VSSPWM is 2.83 kHz when the sampling frequency (f_s) is set to 2 kHz. Thus, the switching frequency of the FVPWM is also set to 2.83 kHz. The simulation is conducted through MATLAB/Simulink with the target of dqz-axis currents and spectrum analyses of phase currents. The configuration of the dual three-phase PMSM is given in Table I. The dc-link voltage is set to 100 V. The cost function (25) is adopted. The average frequency calculation method is to compute the average switch times over a time interval by counting the total number of switch actions. Since there are a total of 12 switches for the six-phase converter, the average switching frequency is written as [22]

$$f_{\text{sw},M}(k) = \frac{1}{12 \cdot 2MT_s} \sum_{i=-M}^{M} \left\| u_{\text{sw}}(k+i) - u_{\text{sw}}(k+i-1) \right\|_1 . \tag{28}$$

The PWM waveforms and the steady-state performances are shown in Figs. 10 and 11 to investigate and compare the performance of these three strategies. Fig. 10 gives the PWM waveforms in sector I. The machine is under steady state with the rated speed of 1200 r/min and with rated currents $i_d = 0$ A, $i_q = 10$ A. All the three methods are with the same average switching frequency of 2.83 kHz. It can be seen that the PWM waveform of conventional FVPWM is asymmetrical, which leads to asymmetrical dqz-axis currents, while the symmetrized FVPWM and VSSPWM are both symmetrical.

Fig. 11 are the results of dq-axis current, dqz-axis currents, phase current, and the phase current spectrum analysis. The peak-to-peak (P-P) values and rms values of dqz-axis currents, and maximum amplitudes near the switching frequency in the phase current spectrum are given in Table II. It can be observed that there are significant reductions of the P-P values and rms values of i_{dz} and i_{qz} for VSSPWM. Particularly, the spectrum analyses show that VSSPWM reduces the amplitude of switching ripples of phase currents by 30.4% and 43.8%, confirming the effect to suppress switching ripples.

The cost value ($\sqrt{i_{dz}^2 + i_{qz}^2}$) represents the total rms value of the $x - y$ current. Fig. 12 shows the comparison of cost

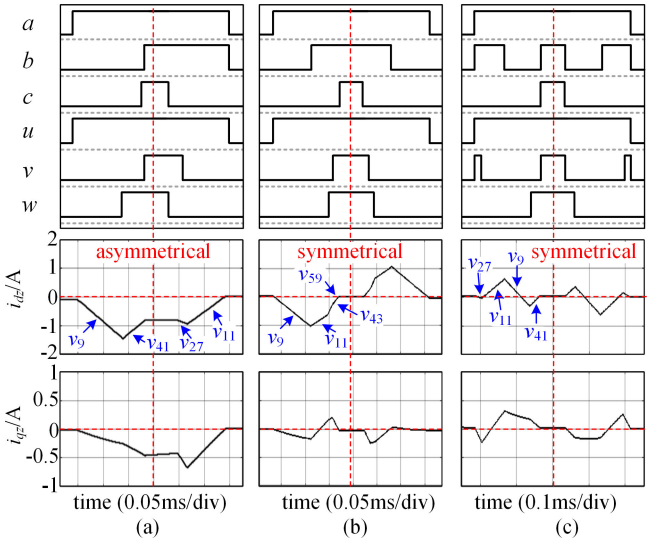

Fig. 10. Simulation PWM waveforms and dqz-axis currents in sector I in one PWM cycle at 100 Hz with the switching frequency of $f_{\text{sw}} = 2.83$ kHz. (a) FVPWM. (b) Symmetrized FVPWM. (c) VSSPWM.

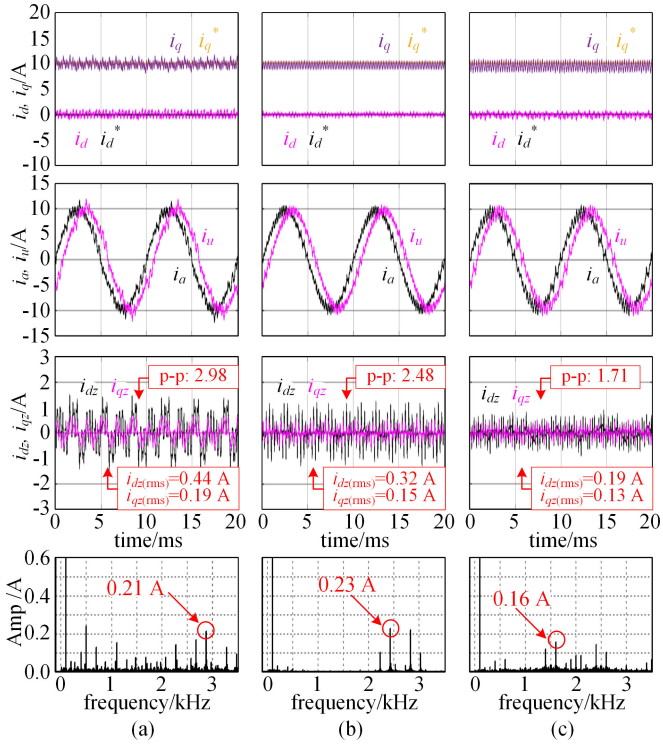

Fig. 11. Simulation results of dq-axis, dqz-axis, and phase a, u currents, and spectrum analyses of phase current a at 100 Hz with the switching frequency of $f_{\text{sw}} = 2.83$ kHz. (a) FVPWM. (b) Symmetrized FVPWM. (c) VSSPWM.

values when machine frequency increases from 30 to 100 Hz for the three strategies. As the speed increases, the costs increase. However, VSSPWM always has the smallest rms values of harmonic currents, which means that VSSPWM has a significant capability to suppress harmonic currents over a wide range of

TABLE II
SIMULATION RESULTS OF THE STEADY-STATE PERFORMANCES OF THE THREE STRATEGIES

	FVPWM	sym. FVPWM	VSSPWM
$i_{dqz(\mathrm{P-P})}$/A	2.98	2.48	1.71
$i_{dz(\mathrm{RMS})}$/A	0.44	0.32	0.19
$i_{qz(\mathrm{RMS})}$/A	0.19	0.15	0.13
Spectrum max. amp/A	0.21	0.23	0.16

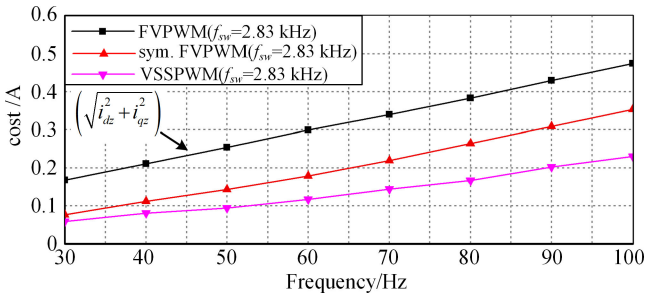

Fig. 12. Comparison of cost values when machine frequency increases from 30 to 100 Hz for the FVPWM with $f_s = f_{\mathrm{sw}} = 2.83$ kHz, symmetrized FVPWM with $f_s = f_{\mathrm{sw}} = 2.83$ kHz, and VSSPWM with $f_s = 2$ kHz, $f_{\mathrm{sw}} = 2.83$ kHz.

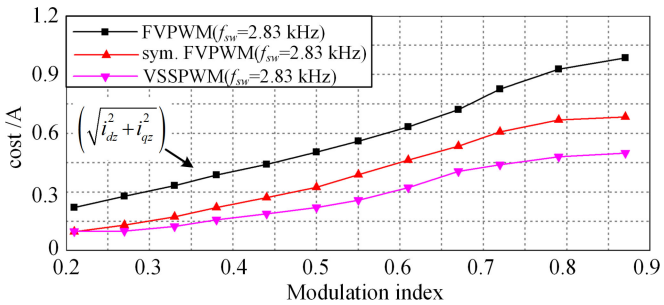

Fig. 13. Comparison of cost values when MI varies for the FVPWM with $f_s = f_{\mathrm{sw}} = 2.83$ kHz, symmetrized FVPWM with $f_s = f_{\mathrm{sw}} = 2.83$ kHz, and VSSPWM with $f_s = 2$ kHz, $f_{\mathrm{sw}} = 2.83$ kHz.

machine speed when all the three methods are with the same switching frequency.

The comparison of cost values when the MI increases from 0.21 to 0.87 for the three strategies is shown in Fig. 13. It can be seen that the proposed method has the lowest cost value among the three approaches, which means it has the best circulating current suppression capability in a wide range of MIs.

V. EXPERIMENTAL RESULTS AND DISCUSSION

In order to verify the effectiveness of proposed VSSPWM, the experiments are performed based on a test bench shown in Fig. 14. The drive system consists of a prototype 12/10 dual three-phase PMSM, a dual three-phase 2-level VSI, a load machine as well as its converter. The parameters of the dual three-phase PMSM are given in Table I. The sampling

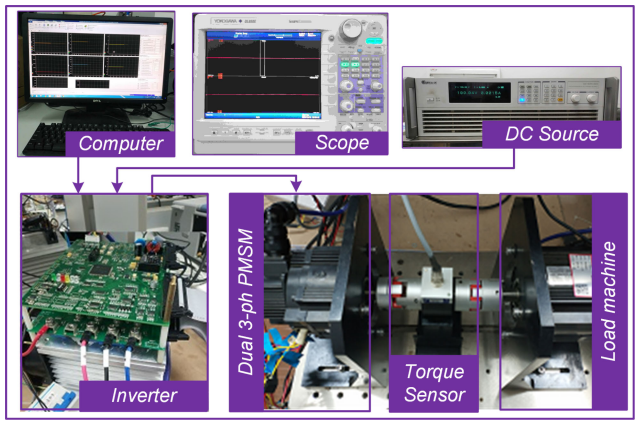

Fig. 14. Test bench.

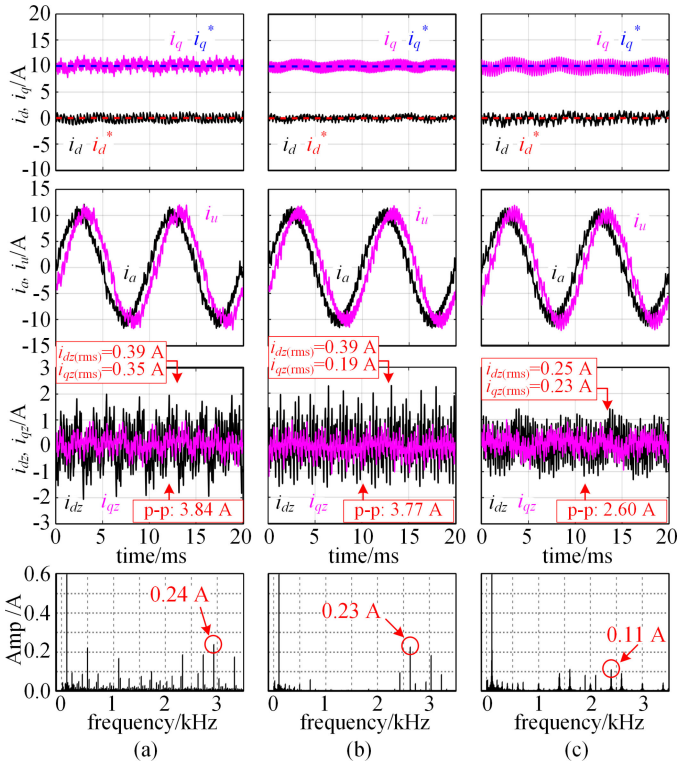

Fig. 15. Experiments results of dq-axis, dqz-axis, and phase a, u currents, and spectrum analyses of phase current a at 100 Hz with the switching frequency of $f_{\mathrm{E}} = 2.83$ kHz. (a) FVPWM. (b) Symmetrized FVPWM. (c) VSSPWM.

frequency of VSSPWM is 2 kHz, and its switching frequency is 2.83 kHz by measuring. The sampling frequency of the comparative conventional FVPWM and symmetrized FVPWM are set to 2.83 kHz for fairness. All the experimental waveforms are recorded from Yokogawa DL850E multiple-channel oscilloscope and repainted with MATLAB.

Fig. 15 gives the dq-, dqz-axis currents, phase currents and the corresponding spectrum analysis results of the three strategies at rated speed of 1200 r/min and rated torque of $i_d = 0$ A, $i_q = 10$ A. Fig. 15(a)–(c) is with the conventional FVPWM, the symmetrized FVPWM, and the proposed VSSPWM, respectively.

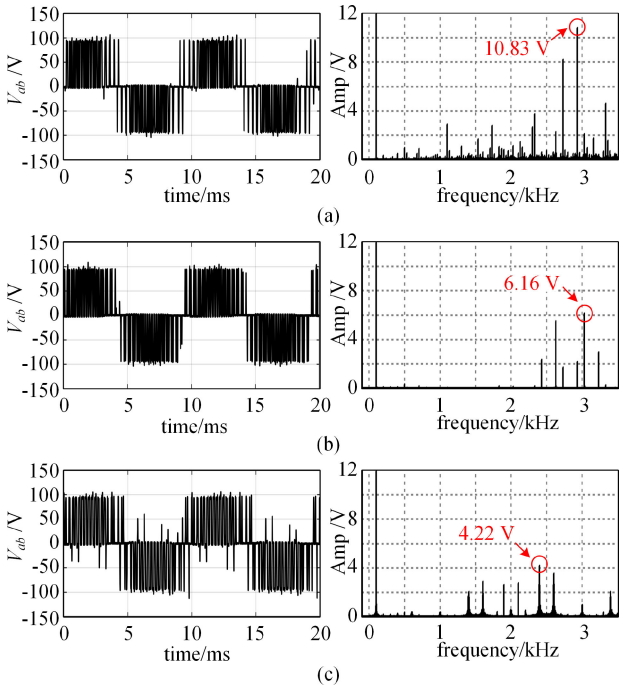

Fig. 16. Experiments results of the line voltage v_{ab} and the corresponding spectrum analyses at 100 Hz with the switching frequency of $f_{\text{sw}} = 2.83$ kHz. (a) FVPWM. (b) Symmetrized FVPWM. (c) VSSPWM.

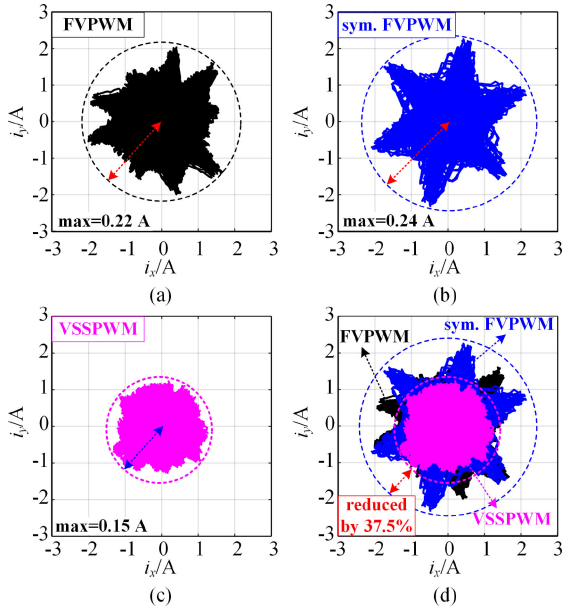

Fig. 17. Trajectories of the i_x–i_y currents of the conventional FVPWM, symmetrized FVPWM, and VSSPWM at 100 Hz with $i_d = 0$ A, $i_q = 10$ A. (a) FVPWM. (b) Symmetrized FVPWM. (c) VSSPWM. (d) Comparison of the three approaches.

The dqz-axis currents' rms values of the three approaches are 0.39 and 0.35 A, 0.39 and 0.19 A, 0.25 and 0.23 A, respectively. The reductions of costs ($\sqrt{i_{dz}^2 + i_{qz}^2}$) by VSSPWM are 35.2% and 21.7%, respectively. VSSPWM reduces P-P values of dqz-axis currents from 3.84 and 3.77 to 2.60 A, with the reductions of 32.3% and 31.0%. Particularly, the spectrum analyses show that VSSPWM reduces the amplitude of phase currents switching ripples from 0.24 and 0.23 to 0.11 A with the reduction of 54.2% and 52.2%, confirming the effect to suppress switching ripples. Although there are significant reduction of dqz-axis currents and switching ripple amplitude, the phase current THD of the three methods are 11.2%, 8.5%, and 11.1%, respectively. In other words, all the performance improvements achieved by VSSPWM are at the expense of a slight increase of phase current distortions.

Fig. 16 gives the line voltage v_{ab} in Fig. 15. It can be seen that VSSPWM reduces the switching ripple amplitudes of the other two methods from 10.83 and 6.16 to 4.22 V, with the reductions of 61.0% and 31.5%.

Fig. 17 depicts the current trajectory of xy-axis current. The size of the enclosed graph of i_x-i_y reflects the fluctuation range of the harmonic currents. The maximum radiuses of the three methods are 0.22, 0.24, and 0.15 A, respectively. The symmetrized FVPWM has the largest radius within the three approaches, while the VSSPWM has the smallest one. VSSPWM reduces the maximum harmonic current fluctuation of symmetrized FVPWM by 37.5%.

Figs. 18 and 19 show the performance comparisons of the three strategies with different load torques and machine speeds.

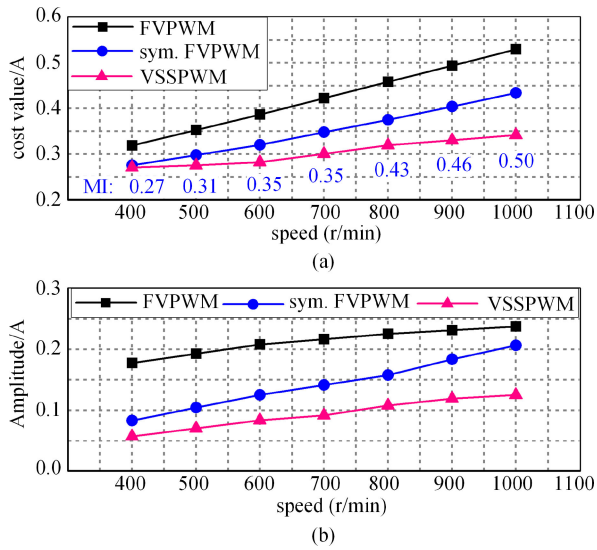

Fig. 18. Comparison of the steady-state performances of the three approaches when the machine speed increases from 500 to 1200 r/min. (a) Cost function values $J = \sqrt{i_{dz}^2 + i_{qz}^2}$. (b) Maximum amplitude of the current harmonics near the switching frequency.

Figs. 18(a) and 19(a) are the cost values $J = \sqrt{i_{dz}^2 + i_{qz}^2}$ comparison results, and Figs. 18(b) and 19(b) are the maximum amplitudes of the harmonic currents near the switching frequency. It can be seen that VSSPWM can effectively reduce the harmonic current rms and the switching current ripple amplitude over a wide range of speeds and a wide range of load torques.

Fig. 20 shows the vibrations of the three strategies at speed of 1 200 r/min. The acceleration of VSSPWM is smaller than that of

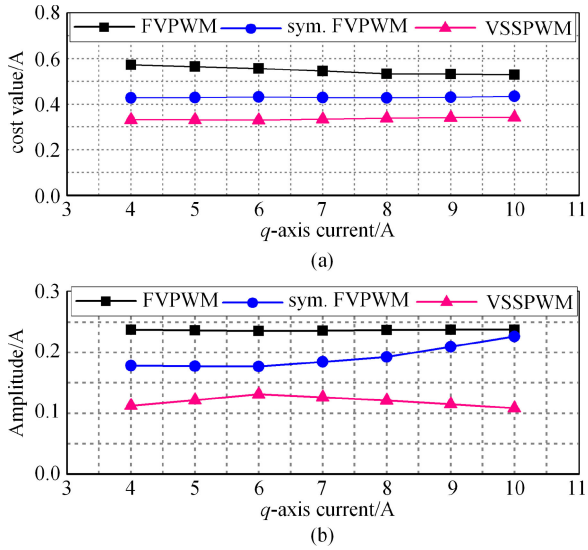

Fig. 19. Comparison of the steady-state performances of the three approaches when the machine load varies ($i_d = 0$, i_q increases from 4 to 10 A). (a) Cost function values $J = \sqrt{i_{dz}^2 + i_{qz}^2}$. (b) Maximum amplitude of the current harmonics near the switching frequency.

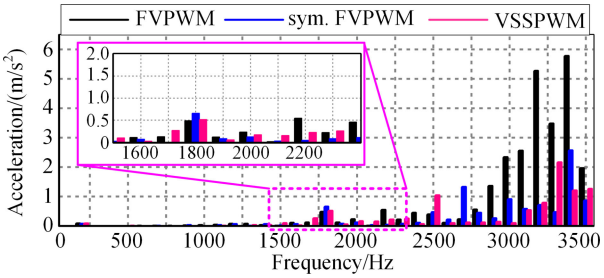

Fig. 20. Vibration analysis comparison of the steady-state performances of the three approaches at 100 Hz.

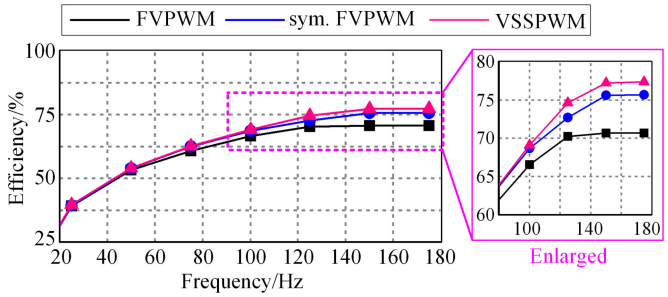

Fig. 21. Efficiency comparison of the three approaches under the steady-state with rated load.

the FVPWM and symmetrized FVPWM in the range of 1 500–2 500 Hz, which is identical to the current spectrum of the three strategies in Fig. 15. Furthermore, the maximum accelerations of the three methods are in the range of 3 000–3 500 Hz due to the resonance with the second-order model, and VSSPWM can also reduce this vibration maximum amplitude compared to the other two strategies. Fig. 21 shows the machine efficiencies with the three strategies with rated load from 25 to 175 Hz. It can be

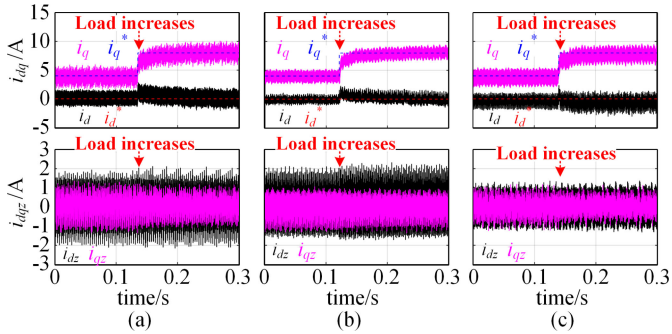

Fig. 22. Comparison of the dynamic performances of the three approaches when the machine load suddenly changed ($i_d = 0$, i_q increases from 4 to 8 A). (a) Conventional FVPWM. (b) Symmetrized FVPWM. (c) VSSPWM.

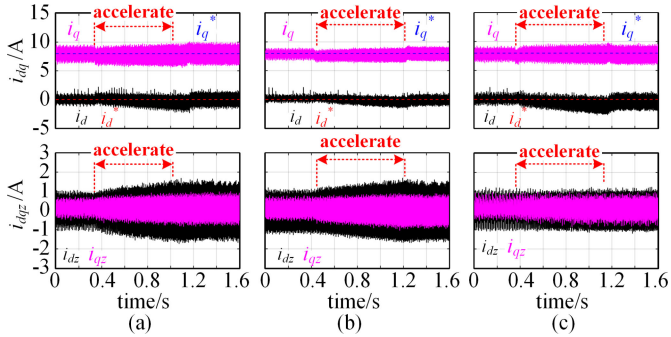

Fig. 23. Comparison of the dynamic performances of the three approaches when the machine speed suddenly changed from 400 to 800 r/min. (a) Conventional FVPWM. (b) Symmetrized FVPWM. (c) VSSPWM.

seen that VSSPWM also improves efficiency. The improvement is not significant when speed is low, however, at high speeds, the efficiency of VSSPWM can be increased by 6.7% and 1.7%, respectively, compared to the other two methods.

Figs. 22 and 23 give the dynamic performances of the three methods when load torque suddenly changes ($i_d^* = 0$, i_q^* changes from 4 to 8 A at 1200 r/min) or machine speed changes (speed changes from 400 to 800 r/min when $i_d^* = 0$, $i_q^* = 8$ A) respectively. It can be seen that during the transient process of load torque variation and speed change, VSSPWM can effectively suppress harmonic current without affecting the performance of dynamic response.

VI. Conclusion

This article proposed a novel variable sequence PWM strategy to suppress high-frequency circulating current harmonics by optimizing switching sequence within one PWM period. The VSSPWM is derived from the basic FVPWM strategy and enumerates the admissible switching sequence patterns. By using a predesigned cost function, the optimal switching sequence can be selected. Compared with traditional FVPWM, the VSSPWM's P-P and rms values of i_{dz} and i_{qz} have been both suppressed significantly over a wide range of machine velocity and load torque. Moreover, the amplitude of the high-frequency current harmonics near the switching frequency has also been reduced.

APPENDIX

The six-dimensional (6-D) electromechanical system can be decomposed into three orthogonal 2-D subplanes: $\alpha-\beta$, $x-y$, and o_1-o_2. The $\alpha-\beta$ subspace contains machine variables (voltage, current, or flux) fundamental component and the harmonics of order $12k\pm1$ ($k=1,2,3,\ldots$). The $x-y$ subspace contains the harmonics of order $6k\pm1$ ($k=1,3,5,\ldots$), while the o_1-o_2 subspace contains harmonics of order $3k$ ($k=1,3,5,\ldots$) [4]. The transformation from natural frame to the stationary $\alpha-\beta-x-y-o_1-o_2$ frame is shown as

$$\left[F_\alpha, F_\beta, F_x, F_y, F_{o_1}, F_{o_2}\right]^{\mathsf{T}} = \boldsymbol{T_6}\cdot\left[F_a, F_b, F_c, F_u, F_v, F_w\right]^{\mathsf{T}}$$

where $\alpha=\pi/6$ and

$$\boldsymbol{T_6} = \sqrt{\frac{1}{3}} \times \begin{bmatrix} 1 & \cos(4\alpha) & \cos(8\alpha) & \cos(\alpha) & \cos(5\alpha) & \cos(9\alpha) \\ 0 & \sin(4\alpha) & \sin(8\alpha) & \sin(\alpha) & \sin(5\alpha) & \sin(9\alpha) \\ 1 & \cos(8\alpha) & \cos(4\alpha) & \cos(5\alpha) & \cos(\alpha) & \cos(9\alpha) \\ 0 & \sin(8\alpha) & \sin(4\alpha) & \sin(5\alpha) & \sin(\alpha) & \sin(9\alpha) \\ 1 & 1 & 1 & 0 & 0 & 0 \\ 0 & 0 & 0 & 1 & 1 & 1 \end{bmatrix}.$$

REFERENCES

[1] X. Lyu, Y. Li, and D. Cao, "DC-link rms current reduction by increasing paralleled three-phase inverter module number for segmented traction drive," *IEEE J. Emerg. Sel. Topics Power Electron.*, vol. 5, no. 1, pp. 171–181, Mar. 2017.

[2] J. Karttunen, S. Kallio, P. Peltoniemi, and P. Silventoinen, "Current harmonic compensation in dual three-phase PMSMs using a disturbance observer," *IEEE Trans. Ind. Electron.*, vol. 63, no. 1, pp. 583–594, Jan. 2016.

[3] F. Barrero and M. J. Duran, "Recent advances in the design, modeling, and control of multiphase machines—Part I," *IEEE Trans. Ind. Electron.*, vol. 63, no. 1, pp. 449–458, Jan. 2016.

[4] Y. Hu, Z. Zhu, and M. Odavic, "Comparison of two-individual current control and vector space decomposition control for dual three-phase PMSM," *IEEE Trans. Ind. Appl.*, vol. 53, no. 5, pp. 4483–4492, Sep./Oct. 2017.

[5] H. S. Che, E. Levi, M. Jones, W.-P. Hew, and N. A. Rahim, "Current control methods for an asymmetrical six-phase induction motor drive," *IEEE Trans. Power Electron.*, vol. 29, no. 1, pp. 407–417, Jan. 2014.

[6] Y. Miyama, M. Ishizuka, H. Kometani, and K. Akatsu, "Vibration reduction by applying carrier phase-shift PWM on dual three-phase winding permanent magnet synchronous motor," *IEEE Trans. Ind. Appl.*, vol. 54, no. 6, pp. 5998–6004, Nov./Dec. 2018.

[7] Y. Luo and C. Liu, "A simplified model predictive control for a dual three-phase PMSM with reduced harmonic currents," *IEEE Trans. Ind. Electron.*, vol. 65, no. 11, pp. 9079–9089, Nov. 2018.

[8] E. A. Klingshirn, "Harmonic filters for six-phase and other multiphase motors on voltage source inverters," *IEEE Trans. Ind. Appl.*, vol. IA-21, no. 3, pp. 588–594, May 1985.

[9] D. Hadiouche, H. Razik, and A. Rezzoug, "On the modeling and design of dual-stator windings to minimize circulating harmonic currents for VSI fed ac machines," *IEEE Trans. Ind. Appl.*, vol. 40, no. 2, pp. 506–515, Mar./Apr. 2004.

[10] A. G. Yepes, J. Doval-Gandoy, F. Baneira, D. Pérez-Estévez, and O. López, "Current harmonic compensation for n-phase machines with asymmetrical winding arrangement and different neutral configurations," *IEEE Trans. Ind. Appl.*, vol. 53, no. 6, pp. 5426–5439, Nov./Dec. 2017.

[11] C. Zhou, G. Yang, and J. Su, "PWM strategy with minimum harmonic distortion for dual three-phase permanent-magnet synchronous motor drives operating in the overmodulation region," *IEEE Trans. Power Electron.*, vol. 31, no. 2, pp. 1367–1380, Feb. 2016.

[12] C. Wang, K. Wang, and X. You, "Research on synchronized SVPWM strategies under low switching frequency for six-phase VSI-fed asymmetrical dual stator induction machine," *IEEE Trans. Ind. Electron.*, vol. 63, no. 11, pp. 6767–6776, Nov. 2016.

[13] Y. Ren and Z.-Q. Zhu, "Reduction of both harmonic current and torque ripple for dual three-phase permanent-magnet synchronous machine using modified switching-table-based direct torque control," *IEEE Trans. Ind. Electron.*, vol. 62, no. 11, pp. 6671–6683, Nov. 2015.

[14] Z. Wang, Y. Wang, J. Chen, and Y. Hu, "Decoupled vector space decomposition based space vector modulation for dual three-phase three-level motor drives," *IEEE Trans. Power Electron.*, vol. 33, no. 12, pp. 10 683–10 697, Dec. 2018.

[15] M. S. A. Shaikh and R. Maurya, "Realization of 24-sector SVPWM with new switching pattern for six-phase induction motor drive," *IEEE Trans. Power Electron.*, vol. 34, no. 6, pp. 5079–5092, Jun. 2019.

[16] D. Jiang and F. Wang, "Current-ripple prediction for three-phase PWM converters," *IEEE Trans. Ind. Appl.*, vol. 50, no. 1, pp. 531–538, Jan./Feb. 2014.

[17] F. Yang, A. R. Taylor, H. Bai, B. Cheng, and A. A. Khan, "Using d–q transformation to vary the switching frequency for interior permanent magnet synchronous motor drive systems," *IEEE Trans. Transp. Electrific.*, vol. 1, no. 3, pp. 277–286, Oct. 2015.

[18] Q. Li and D. Jiang, "Variable switching frequency PWM strategy of two-level rectifier for dc-link voltage ripple control," *IEEE Trans. Power Electron.*, vol. 33, no. 8, pp. 7193–7202, Aug. 2018.

[19] Y. Hu, Z.-Q. Zhu, and K. Liu, "Current control for dual three-phase permanent magnet synchronous motors accounting for current unbalance and harmonics," *IEEE J. Emerg. Sel. Topics Power Electron.*, vol. 2, no. 2, pp. 272–284, Jun. 2014.

[20] S. Kallio, M. Andriollo, A. Tortella, and J. Karttunen, "Decoupled dq model of double-star interior-permanent-magnet synchronous machines," *IEEE Trans. Ind. Electron.*, vol. 60, no. 6, pp. 2486–2494, Jun. 2013.

[21] I. Gonzalez-Prieto, M. J. Duran, J. J. Aciego, C. Martin, and F. Barrero, "Model predictive control of six-phase induction motor drives using virtual voltage vectors," *IEEE Trans. Ind. Electron.*, vol. 65, no. 1, pp. 27–37, Jan. 2018.

[22] B. Stellato, T. Geyer, and P. J. Goulart, "High-speed finite control set model predictive control for power electronics," *IEEE Trans. Power Electron.*, vol. 32, no. 5, pp. 4007–4020, May 2016.

Donglin Ye (S'17) was born in Hubei, China. He received the B.E.E. degree in electrical engineering in 2015 from the Huazhong University of Science and Technology, Wuhan, China, where he is currently working toward the Ph.D. degree in electrical engineering with the School of Electronic and Electrical Engineering.

His research interests include control strategy of PM machines and multiphase machines.

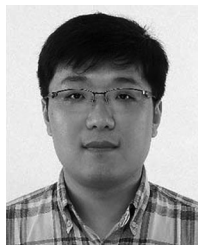

Jian Li (M'10–SM'18) received the B.E.E. degree from the Dalian University of Technology, Dalian, China, in 2005, and the M.S.E.E. and Ph.D. degrees from Dong-A University, Busan, South Korea, in 2007 and 2011, respectively, in electrical engineering.

Since 2013, he has been an Associate Professor with the Department of Electrical Machine and Drive Engineering, Huazhong University of Science and Technology, Wuhan, China. He has authored a total of 67 SCI papers in IEEE TRANSACTIONS ON INDUSTRIAL ELECTRONICS, IEEE TRANSACTIONS ON POWER ELECTRONICS, IEEE TRANSACTIONS ON INDUSTRY APPLICATIONS, etc., among which 32 are with first and corresponding authorship. He received 14 invention patents (11 with first authorship). His research interests include high torque density axial flux motors, wide speed range high-efficiency variable flux traction motors, and high-power traction drives. He is the recipient of Best Paper Award from 2014 and 2018 ICEMS.

Ronghai Qu (S'01–M'02–SM'05–F'17) was born in China. He received the B.E.E. and M.S.E.E. degrees in electrical engineering from Tsinghua University, Beijing, China, in 1993 and 1996, respectively, and the Ph.D. degree in electrical engineering from the University of Wisconsin–Madison, Madison, WI, USA, in 2002.

In 1998, he joined as a Research Assistant at the Wisconsin Electric Machines and Power Electronics Consortiums, Madison, WI, USA. In 2002, he was a Senior Electrical Engineer with Northland, a Scott Fetzer Company, Watertown, NY, USA. Since 2003, he has been a Senior Electrical Engineer with the Electrical Machines and Drives Laboratory, General Electric Global Research Center, Niskayuna, NY, USA. Since 2010, he has been a Professor with the Huazhong University of Science and Technology, Wuhan, China. He has authored more than 120 published technical papers and is the holder of more than 50 patents/patent applications.

Dr. Qu is a Full Member of Sigma Xi. He was the recipient of several awards from the GE Global Research Center, since 2003, including the Technical Achievement and Management Awards. He was also the recipient of the 2003 and 2005 Best Paper Awards, Third Prize, from the Electric Machines Committee of the IEEE Industry Applications Society (IAS) at the 2002 and 2004 IAS Annual Meetings.

Dong Jiang (S'05–M'12–SM'16) received the B.S. and M.S. degrees in electrical engineering from Tsinghua University, Beijing, China, in 2005 and 2007, respectively. He started working toward the Ph.D. degree in high density motor controller from the Center for Power Electronics Systems, Virginia Tech, Blacksburg, VA, USA, in 2007, and was transferred with his advisor in 2010 to the University of Tennessee, Knoxville, TN, USA, where he received the Ph.D. degree in December 2011.

From January 2012 to July 2015, he was a Senior Research Scientist/Engineer with the United Technologies Research Center, Connecticut. Since July 2015, he has been a Professor with the Huazhong University of Science and Technology, Wuhan, China. His research interests include power electronics and motor drives, with more than 100 authored or coauthored IEEE journal and conference papers in this area.

Dr. Jiang is currently an Associate Editor for the IEEE TRANSACTIONS ON INDUSTRY APPLICATIONS. He was the recipient of two Best Paper Awards in IEEE conferences.

Lifan Xiao (S'17) received the B.S. degree in electrical engineering in 2015 from the Huazhong University of Science and Technology, Wuhan, China, where he is currently working toward the Ph.D. degree in electric and electronic engineering.

His research interests include motor drives, modulation method, and control of machines with low-switching frequency for traction usage.

Yang Lu (S'16) was born in Hubei, China, in 1993. He received the B.E.E. degree in energy and power engineering from North China Electrical Power University, Hebei, China, in 2015. He is currently working toward the Ph.D. degree in electrical engineering with the State Key Laboratory of Advanced Electromagnetic Engineering and Technology, School of Electronic and Electrical Engineering, Huazhong University of Science and Technology, Wuhan, China.

His research interests include the design and analysis of permanent-magnet machines, reluctance machines, with a special focus on the vibration and noise of PMSMs.

Junhua Chen (S'15–M'18) received the B.E.E. and the Ph.D. degrees in electrical engineering from the Huazhong University of Science and Technology, Wuhan, China, in 2013 and 2018, respectively.

He is currently a Postdoctoral Fellow with the Huazhong University of Science and Technology. His research interests include control of PM machines and power electronics, design and analysis of permanent-magnet machines, and reluctance machines, with a special focus on the vibration and noise of PMSMs.